Radial Spin Texture in Elemental Tellurium with Chiral Crystal Structure

M. Sakano, M. Hirayama, T. Takahashi, S. Akebi, M. Nakayama, K. Kuroda, K. Taguchi, T. Yoshikawa, K. Miyamoto, T. Okuda, K. Ono, H. Kumigashira, T. Ideue, Y. Iwasa, N. Mitsuishi, K. Ishizaka, S. Shin, T. Miyake, S. Murakami, T. Sasagawa, and Takeshi Kondo

Phys. Rev. Lett. **124**, 136404 — Published 30 March 2020

DOI: 10.1103/PhysRevLett.124.136404

Radial spin texture in elemental tellurium with chiral crystal structure

M. Sakano[1,2], M. Hirayama[3,4,5], T. Takahashi[6], S. Akebi[1], M. Nakayama[1], K. Kuroda[1], K. Taguchi[7], T. Yoshikawa[7], K. Miyamoto[8], T. Okuda[8], K. Ono[9], H. Kumigashira[9,10], T. Ideue[2], Y. Iwasa[2,5], N. Mitsuishi[2], K. Ishizaka[2,5], S. Shin[1,11], T. Miyake[12], S. Murakami[3,4], T. Sasagawa[6], and Takeshi Kondo[1,11]

[1]Institute for Solid State Physics (ISSP), The University of Tokyo, Kashiwa, 277-8581, Japan

[2]Quantum-Phase Electronics Center (QPEC) and Department of Applied Physics, The University of Tokyo, Bunkyo-ku, Tokyo, 113-8656, Japan

[3]Department of Physics, Tokyo Institute of Technology, Meguro-ku, Tokyo, 152-8551, Japan

[4]Tokodai Institute for Element Strategy (TIES), Tokyo Institute of Technology, Meguro-ku, Tokyo, 152-8551, Japan

[5]RIKEN Center for Emergent Matter Science (CEMS), Wako, Saitama, 351-0198, Japan

[6]Materials and Structures Laboratory (MSL), Tokyo Institute of Technology, Yokohama, Kanagawa, 226-8503, Japan.

[7]Graduate School of Science, Hiroshima University, Higashi-Hiroshima, Hiroshima, 739-8526, Japan

[8]Hiroshima Synchrotron Radiation Center (HiSOR), Hiroshima University, Higashi-Hiroshima, Hiroshima, 739-0046, Japan

[9]Institute of Materials Structure Science, High Energy Accelerator Research Organization (KEK), Tsukuba, Ibaraki 305-0801, Japan

[10]Institute of Multidisciplinary Research for Advanced Materials (IMRAM), Tohoku University, Sendai 980-8577, Japan

[11]AIST-UTokyo Advanced Operando-Measurement Technology Open Innovation Laboratory (OPERANDO-OIL), Kashiwa, Chiba 277-8581, Japan

[12] Research Center for Computational Design of Advanced Functional Materials (CD-FMat), AIST, Tsukuba, Ibaraki, 305-8568, Japan

The chiral crystal is characterized by a lack of mirror symmetry and inversion center, resulting in the inequivalent right- and left-handed structures. In the noncentrosymmetric crystal structure, the spin and momentum of electrons are expected to be locked in the reciprocal space with the help of the spin-orbit interaction. To reveal the spin textures of chiral crystals, we investigate the spin and electronic structure in a *p*-type semiconductor, elemental tellurium, with the simplest chiral structure by using spin- and angle-resolved photoemission spectroscopy. Our data demonstrate that the highest valence band crossing the Fermi level has a spin component parallel to the electron momentum around the Brillouin zone corners. Significantly, we have also confirmed that the spin polarization is reversed in the crystal with the opposite chirality. The results indicate that the spin textures of the right- and left-handed chiral crystals are hedgehog-like, leading to unconventional magnetoelectric effects and nonreciprocal phenomena.

Knowledge of crystal lattice symmetries helps us to understand the physical phenomena and properties of materials. In a chiral crystal, the electricity and magnetism are known to mutually coupled, as first discovered by Arago in 1811 [1] for alpha-quartz showing the natural optical activity. The chiral crystal structure is defined by the lack of mirror symmetry, giving rise to two inequivalent crystals, so-called right- and left-handed crystals, which show opposite physical responses in the magnetoelectric effect [2,3]. This structure is also intriguing in that the spin degeneracy should be lifted in momentum space (**k**-space), even in nonmagnetic materials, by the combination of the spin-orbit interaction (SOI) and the breaking of inversion symmetry [4,5,6]. Recently, Tsirkin *et al*. have revealed that the spin-orbit coupled bands of chiral crystals, which cross at the time-reversal invariant momenta (called Kramers-Weyl fermions [7]), can play an important role in various gyrotropic effects [8]. Several calculational studies on the nonmagnetic chiral materials have predicted that the spin components parallel to the momenta of electrons should appear all-around the highly symmetrical **k**-points [7,9-12]. However, the experimental verification of the theoretically predicted spin-polarized states in a chiral nonmagnetic crystal is still lacking, thus it has been strongly desired in condensed matter physics; notably, this purpose requires the challenging demonstration of a one-to-one correspondence between the handedness of the chirality and the direction of spin-polarization in the band. We also note that there has been so far only a handful of reports [13-15] on the direct observation of spin-polarized states for bulk bands of three-dimensional (3D) materials because of its difficulty, contrasting to many pieces of research for the surface properties related to Rashba or topological states.

The elemental tellurium is the simplest material with a chiral structure [16] consisting of atomic spiral chains along the *z*-axis (see Figs. 1(a) and 1(b) for the right-handed case). The band structure has been established before the 1970s by theoretical [7,17-23] and experimental [24-27] studies, which identified a gap size of 0.32 eV [24,28] and the valence band maxima (VBM) located slightly off the *H*- and *H'*-point [Fig. 1(f)]. The spin degeneracy at the top of valence bands which crosses the Fermi level (E_F) is lifted [24] because of the combination of the SOI of tellurium 5*p* orbitals and the noncentrosymmetric crystal structure; this property could trigger the electromagnetic effects (e.g., the current-induced optical activity [29,30] and magnetization in bulk [31]). Recently, the Weyl semimetal phase was suggested by Hirayama *et al.* to emerge under the hydrostatic pressure when the spin-polarized conduction and valence bands are inverted across the band-gap around the Brillouin zone (BZ) corners. This topological property possibly leads to exotic phenomena induced by the spin-momentum locked electronic structure [22,23].

In this work, we experimentally realize, for the first time, the characteristic spin-momentum locking in the band structure of chiral crystals, by investigating elemental tellurium, which has the simplest chiral crystal structure with the space group $P3_121$ (right-handed crystal) as shown in Figs. 1(a) and 1(b), or $P3_221$ (left-handed crystal) [16]. Significantly, we reveal a hedgehog-like radial spin texture, which is reversed in the spin polarization for the opposite chirality. The spin magnetic moments observed on the Fermi surface offer excellent potential for spintronic applications.

The $h\nu$-dependent ARPES measurements ($h\nu$ = 63-93 eV) were performed at BL28 in Photon Factory, KEK, with total energy-resolution of 25-40 meV. SARPES measurements ($h\nu$ = 18 eV, *p*-polarized light) were performed at ESPRESSO end station of BL-9B in the Hiroshima Synchrotron Radiation Center (HiSOR) [32,33,34]; the angular resolution was set to ±1.5°, and the total energy-resolution was set to 60 meV. Single crystals of tellurium were grown by the physical vapor transport technique [35]. The hole carrier densities were estimated from the Hall coefficient to be in the *p*-type semiconducting regime of 1.6×10^{15}-6.0×10^{17} cm^{-3}, which is consistent with the previous studies [24]. The samples were cleaved *in situ* along the (10-10) plane and measured at 20 K. We calculated the fully-relativistic electronic structure based on the density function theory by a first-principles code QMAS (Quantum MAterials Simulator [36]), and the GW correction [37,38] was added (see the supplementary of ref. [23] for details of the calculation conditions).

We have determined the chirality of the crystals used for ARPES and SARPES measurements by observing the asymmetric etch pits formed by the hot concentrated sulfuric acid (red frames in Figs. 1(d) and 1(e) for the right- and left-handed crystals, respectively) [39-41]. While the band structure we obtained by ARPES is for the bulk state, a two-dimensional BZ projected on the cleavage plane is also denoted for convenience in Fig. 1(f) (a blue rectangle) together with the main three-dimensional BZ (thick black lines). The $h\nu$-dependent ARPES measurements were performed along the purple cut ($\bar{\Gamma}$-$\bar{H}$) on the two-dimensional BZ [Fig. 1(f)], which traces the shaded plane (Γ-*M*-*H*) in the three-dimensional BZ [see Figs. 1(f) and 1(g)].

Figures 2(a)-2(f) show the ARPES dispersions measured at various $h\nu$s along $\bar{\Gamma}$-$\bar{H}$ for the left-handed crystal. These clearly exhibit a $h\nu$ dependence (or a k_x dependence) in the band dispersions, indicating that our data capture the bulk state. The top of the band at $\bar{H}$-point shifts up toward higher energies with decreasing $h\nu$, and it crosses E_F at $h\nu$ = 63 eV [Fig. 2(f)], which corresponds to the *H*-point in the three-dimensional BZ [Fig. 1(g)] [27]. The hole-like bands are further examined in Figs. 2(g)-2(i) by mapping the ARPES intensities across the *H*-point at several binding energies [red broken lines in Fig. 2(m)]. The corresponding calculations are also plotted next to each panel of the ARPES data in Figs. 2(j)-2(l); here, the career number is fixed to the experimental value, which locates E_F to 20 meV below VBM. At E_F [Fig. 2(g)], faint but finite ARPES intensities are observed near the *H*-point, indicating the formation of a tiny Fermi pocket expected by calculations [Fig. 2(j)]. The equi-energy surface becomes larger at lower energies owing to the hole-like band. In addition, the inner intensities appear at E–E_F = –0.15 eV [a red dashed circle in Fig. 2(h)], and the double-contours eventually get clearer at deeper binding energies [E–E_F = –0.30 eV in Fig. 2(i)], agreeing with calculations [Figs. 2(k) and 2(l)]; here, we note that the ARPES image looks blurred, likely because the ARPES intensities are integrated over the resolution window of energy and momentum ($\delta\varepsilon$ and δk). Notably, the surface-sensitive probe causes δk to become large in the k_x direction perpendicular to the cleavage surface, yielding a vague feature in the intensity mapping of Figs. 2(h) and 2(i).

The overall hole-like band across the *H*-point is demonstrated in Fig. 2(m) by plotting the E-k_z image of ARPES. The highest valence band has a concave shape with the energy maximum slightly off the *H*-point, and it crosses E_F, whereas the second-highest band has a top below E_F (E–E_F = -0.15 eV) just at *H*-point. The dispersions observed down to E–E_F = –2.0 eV [Fig. 2(m)] agree with the calculations [Fig. 2(n)], and these are assigned to six lone-pair states (H_4, H_5, and four H_6 bands) by considering the spin degree of freedom. The highest and second-highest bands are described by double group representations (H_4, and H_5, respectively) [18,19,24], and thus the spin degeneracy of these is lifted. While the D_3 symmetry requires no net spin polarization at the highly symmetrical *H*-point, non-zero spin polarization is expected to appear off the *H*-point [8,23,27,31].

To reveal spin polarizations for the valence bands, we have performed SARPES experiment at $h\nu$ = 18 eV, in which the highest and second-highest bands were clearly observed [Fig. 3(e)]. Figures 3(b)-3(d) show the SARPES spectra for the left-handed crystal, measured at the **k**-points around the *H*-point indicated as #1-#13 in Figs. 3(a) and 3(e) (emission angles from -9.0 deg. to 9.0 deg.); each panel corresponds to the x, y, and z component of the spin magnetic moment [m_x, m_y, and m_z, respectively] defined parallel to the orthogonal axes in Figs. 1(a) and 1(b). Significantly, the spectra for m_z [Fig 3(d)] show a clear difference between the spin-up (red) and spin-down (blue) intensities, and the relationship between the two is reversed across the *H*-point (#7, or the zero-emission angle). These contrasts to the other components (m_x and m_y), which show nearly equivalent intensities for the spin-up and spin-down. Since the measured **k**-points of #1-#13 [blue circles in Fig. 3(a)] are aligned nearly parallel to the k_z direction, our SARPES results demonstrate the hedgehog-like radial spin texture formed around the *H*-point in the highest valence band, which is characteristic in a chiral crystal structure.

The spin-polarized band dispersion experimentally determined is exhibited in Fig. 3(f), which maps the z component (P_z) of spin polarization corresponding to the ARPES image in Fig. 3(e). The red and blue circles in the panel plot the peak positions marked in Fig. 3(d) for the SARPES spectra of m_z. The data clearly illustrates the outward and inward radial spin textures in the highest and second-highest bands, respectively, agreeing with the calculations along *K*-*H*-*K* (or k_z direction) in Fig. 3(g). The spin polarizations are represented by the different areas of open red/blue circles in Fig. 3(g), which estimate about $\pm$55% and $\pm$90% at VBM ($\pm$0.02 Å^{-1} off the *H*-point) and at E_F (20 meV below VBM), respectively.

The *H*'-point is another BZ corner inequivalent with the *H*-point, and thus the same outward radial spin textures are expected around it for the left-handed crystal, since these two points are mutually linked by the time-reversal and D_3 symmetry. Our experiments have indeed confirmed it, as demonstrated in Fig. 3(h): the upper and middle SARPES spectra obtained at #5' and #5' close to the *H'*- and *H'*-point, respectively, are almost identical. To further demonstrate the specific feature in chiral crystals, we have also measured a crystal with the opposite chirality (a right-handed crystal).

Very importantly, the z-oriented spin polarizations are observed to be completely inverted from that in the left-handed crystal [see the lower spectra in Fig. 3(h) measured at #5], indicating that the radial spin textures around the H- and H'-points are inward in the case of the right-handed crystal [8,42].

Figures 4(a) and 4(b) show the calculated Fermi surfaces along the k_y-k_z plane around the H-point for the right- and left-handed crystals, respectively. The arrows represent the polarization directions of spin magnetic moment projected on the y-z plane along the Fermi surface. The upper and lower numbers nearby each arrow describes the absolute values of the spin polarizations projected on the y-z plane ($|P_{yz}|$) and along the x-direction (P_x), respectively. In both the crystals, the spin textures are the same between the regions around the H- and H'-points, which are linked by the time-reversal symmetry. Since the radial spin textures are inward and outward in the right- and left-handed crystals, respectively, the BZ corners (the H- and H'-points) behave as if being either a sink or source of the effective magnetic field like a monopole, depending on the crystal chirality.

The spin polarization of about ±90% nearly parallel to the z-direction is realized along the longer direction of the dumbbell-shaped Fermi surface. In contrast, the spin polarization along the shorter direction is non-zero but small. Interestingly, the tellurium atomic chain can be viewed as a solenoid, which applies an effective magnetic field along the z-axis to an electron traveling in the k_z direction. Thus, the non-zero spin components around the symmetrical **k**-points should originate from the peculiar symmetry of the chiral crystal structure, which lacks the mirror symmetry.

Finally, we discuss the spin and electronic structures just at H- and H'-point. With the D_3 symmetry, the net spin polarization must be absent in **k**-space. However, the SOI plays an essential role in coupling the spin and orbital degrees of freedom, and it lifts the degeneracy of the spin into two irreducible representations of the double groups H_4 and H_5 in Fig. 4(c). Figures 4(d) and 4(e) show the real-space views of the spin texture on the atomic spiral chain of tellurium symmetrically allowed under the D_3 symmetry for the highest and second-highest valence bands at the H-point for the right-handed crystal. While the net spin polarization is canceled to be zero, the in-plane outward (inward) radial spin texture in real space is realized vertically to the z-axis for H_4 (H_5) state, and it behaves as if consisting of local spin magnetic moments denoted by the red and blue arrows in Fig. 4(d) [Fig. 4(e)]. On the other hand, the real-space spin textures for electronic structure just at the inequivalent H'-point should be inverted from those around the H-point due to the time-reversal symmetry, and again, no net magnetic moment is obtained in real- and **k**-spaces. Such lifting of the spin degeneracy without net spin polarization universally occurs via SOI in the materials belonging to the D_3 point group.

To summarize, the spin texture of a chiral nonmagnetic crystal was experimentally verified for the first time by the ARPES and SARPES measurements of the elemental trigonal tellurium, which is the simplest material with a chiral structure. Observation of radial spin texture, which becomes inward or outward depending on the winding direction of spiral tellurium-chains, gave a one-to-one correspondence to the chirality of the crystal structure.

This research was partly supported by CREST projects (Grant No. JPMJCR16F2, No.

JP-MJCR14F1) from Japan Science and Technology Agency (JST) and JSPS KAKENHI (Grants-in-Aid for Scientific Research) (Grant No. JP18H03678, JP19H00651). We thank T. Itou and T. Furukawa for fruitful discussion.

References

1. L. D. Barron, Chirality **24**, 879 (2012).

2. N. B. Baranova, Yu. V. Boddanov, and B. Ya. Zel'Dovich, Opt. Commun. **22**, 243 (1977).

3. V. I. Belinicher and B. I. Sturman, Sov. Phys. Usp. **23**, 199 (1980).

4. G. Dresselhaus, Phys. Rev. **100**, 580 (1955).

5. E. I. Rashba, Sov. Phys. Solid. State **1**, 368-380 (1959).

6. R. C. Casella, Phys. Rev. Lett. **5**, 371 (1960).

7. G. Chang, B. J. Wieder, F. Schindler, D. S. Sanchez, I. Belopolski, S.-M. Huang, B. Singh, D. Wu, T.-R. Chang, T. Neupert, S.-Y. Xu, H. Lin, and M. Z. Hasan, Nat. Mater. **17**, 978 (2018).

8. S. S. Tsirkin, P. A. Puente, and I. Souza, Phys. Rev. B **97**, 035158 (2018).

9. A. Nakamura, H. Harima, M. Hedo, T. Nakata, and Y. Onuki, J. Phys. Soc. Jpn. **82**, 113705 (2013).

10. Y. Onuki, A. Nakamura, T. Uejo, A. Teruya, M. Hedo, T. Nakama, F. Honda, and H. Harima, J. Phys. Soc. Jpn. **83**, 061018 (2014).

11. H. Harima, T. Goho, and T. Tomi, J. Phys: Conf. Series **592**, 012040 (2015).

12. T. Yoda, T. Yokoyama, and S. Murakami, Sci. Rep. **5**, 12024 (2015).

13. K. Ishizaka, M. S. Bahramy, H. Murakawa, M. Sakano, T. Shimojima, T. Sonobe, K. Koizumi, S. Shin, H. Miyahara, A. Kimura, K. Miyamoto, T. Okuda, H. Namatame, M. Taniguchi, R. Arita, N. Nagaosa, K. Kobayashi, Y. Murakami, R. Kumai, Y. Kaneko, Y. Onose, and Y. Tokura, Nat. Mater. **10**, 521 (2011).

14. R. Suzuki, M. Sakano, Y. J. Zhang, R. Akashi, D. Morikawa, A. Harasawa, K. Yaji, K. Kuroda, K. Miyamoto, T. Okuda, K. Ishizaka, R. Arita, and Y. Iwasa, Nat. Nanotechnol. **9**, 611 (2014).

15. J. Krempaský, H. Volfová, S. Muff, N. Pilet, G. Landolt, M. Radović, M. Shi, D. Kriegner, V. Holý, J. Braun, H. Ebert, F. Bisti, V. A. Rogalev, V. N. Strocov, G. Springholz, J. Minár, and J. H. Dil, Phys. Rev. B **94**, 205111 (2016).

16. A. J. Bradley, *Phil. Mag.* **48**, 477 (1924).

17. J. R. Reitz, Phys. Rev. **105**, 1233 (1957).

18. M. Hulin, J. Phys. Chem. Solids **27**, 441 (1966).

19. T. Doi, K. Nakao, and H. Kamimura, J. Phys. Soc. Jpn. **28**, 36 (1970).

20. J. D. Joannopoulos, M. Schlüter, and M. L. Cohen, Phys. Rev. B **11**, 2186 (1976).

21. H. Peng. N. Kioussis, and G. J. Snyder, Phys. Rev. B **89**, 195206 (2014).

22. L. A. Agapito, N. Kioussis, W. A. Goddard III, and N. P. Ong, Phys. Rev. Lett. **110**, 176401 (2013).

23. M. Hirayama, R. Okugawa, S. Ishibashi, S. Murakami, and T. Miyake, Phys. Rev. Lett. **114**, 206401 (2015).

24. R. S. Caldwell, and H. Y. Fan, Phys. Rev. **114**, 664 (1959).

25. D. Hardy, and C. Rigaux, Solid State Commun. **5**, 889 (1967).

26. L. D. Laude, B. Fitton, and M. Anderegg, Phys. Rev. Lett. **26**, 637 (1971).

27. K. Nakayama, M. Kuno, K. Yamauchi, S. Souma, K. Sugawara, T. Oguchi, T. Sato, and T. Takahashi, Phys. Rev. B **95**, 125204 (2017).

28. V. B. Anzin, M. I. Eremets, Yu. V. Hosichkin, A. I. Nadezhdinskii, and A. M. Shirokov, phys. Status Solidi (a) **42**, 385 (1977).

29. E. L. Vorob'ev, E. L. Ivchenko, G. E. Pikus, I. I. Farbshtein, V. A. Shalygin, and A. V. Shuturbin JETP Lett. **29**, 441 (1979).

30. V. A. Shalygin, A. N. Sofronov, L. E. Vorob'ev, and I. I. Farbshtein, Phys. Solid State **54**, 2362 (2012).

31. T. Furukawa, Y. Shimokawa, K. Kobayashi, and T. Itou, Nat. Commun. **8**, 954 (2017).

32. T. Okuda, K. Miyamoto, H. Miyahara, K. Kuroda, A. Kimura, H. Namatame, and M. Taniguchi, Rev. Sci. Instrum. **82**, 103302 (2011).

33. T. Okuda, J. Phys.: Condens. Matter **29,** 483001 (2017).

34. See Supplemental Material at http://link.aps.org/supplemental/xxxxxx for the experimental condition of the SARPES measurement in details.

35. T. Ideue, M. Hirayama, H. Taiko, T. Takahashi, M. Murase, T. Miyake, S. Murakami, T. Sasagawa, and Y. Iwasa, Proc. Natl. Acad. Sci. **116**, 25530 (2019).

36. http://qmas.jp/

37. M. Van Schilfgaarde, T. Kotani, and S. V. Faleev, Phys. Rev. B **74**, 245125 (2006).

38. T. Miyake and F. Aryasetiawan, Phys Rev B **77**, 085122 (2008).

39. L. C. Lovell, J. H. Wernick, and K. E. Benson, Acta. Met. **6**, 716 (l958).

40. J. S. Blakemore, and K. C. Nomura, J. appl. Phys. **32**, 745 (1961).

41. A. Koma, E. Takimoto, and S. Tanaka, phys. stat. sol. **40**, 239 (1970).

42. Y. Tanaka, S. P. Collins, S. W. Lovesey, M. Matsumami, T. Moriwaki, and S. Shin, J. Phys. Condens. Matter **22**, 122201 (2010).

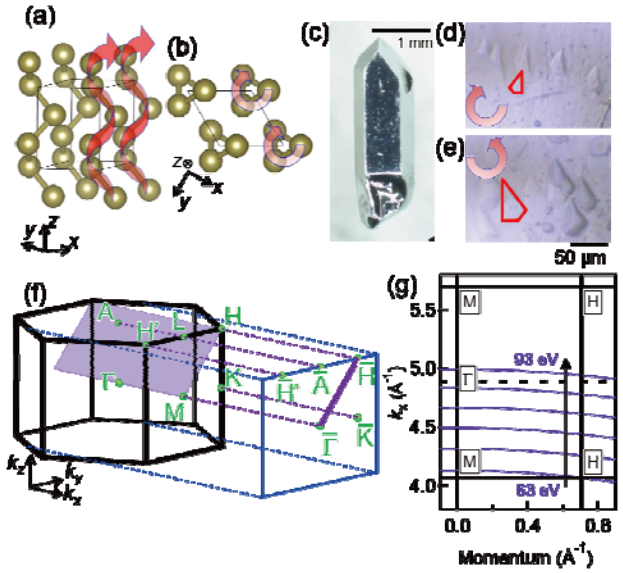

FIG. 1. (a) Crystal structure with a right-handed screw axis (space group $P3_121$). (b) Bottom view of the right-handed crystal. (c) Picture of the single crystal. (d), (e) Optical micrograph images of etch pits represented by the red shapes for the right- and left-handed crystals、respectively. (f) The first Brillouin zone (thick black lines), and the corresponding two-dimensional one projected on the cleavage plane (thin blue lines). The purple line (-) in the cleavage plane indicates the orientation of measurement by ARPES in Fig. 2. The shaded region (H-M-Γ) can be traced by changing photon energies ($h\nu$s) (g) Momentum cuts (purple lines) for various $h\nu$s ($h\nu$ = 63-93 eV) on the shaded plane in (f). The inner potential of V_0 = 6.4 eV was used to estimate the k_x values.

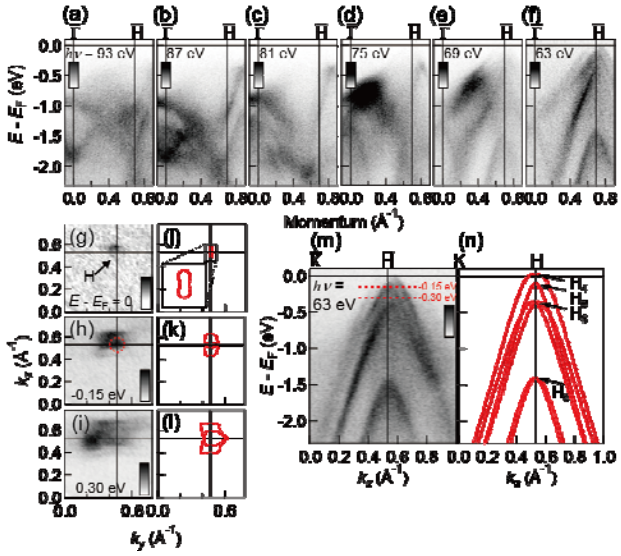

FIG. 2. (a)-(f) The ARPES images along - measured over a wide range of $h\nu$ = 93-63 eV. The corresponding momentum cuts are represented in Fig. 1(g). (g)-(i) ARPES intensity map along k_y-k_z at the constant energies of E–E_F = 0, –0.15, and –0.30 eV, respectively. The data are recorded at $h\nu$ = 63 eV, crossing the H-point [Fig. 1(g)]. (j)-(l) Energy contours of calculated valence bands corresponding to (g)-(i), respectively; here the Fermi level is set to 20 meV below VBM for the career number of 6.0×10^{17} cm^{-3}. The inset in (j) shows a magnified view of the Fermi surface. (m) E-k_z ARPES image recorded at $h\nu$ = 63 eV. (n) Calculated band dispersions along K-H-K.

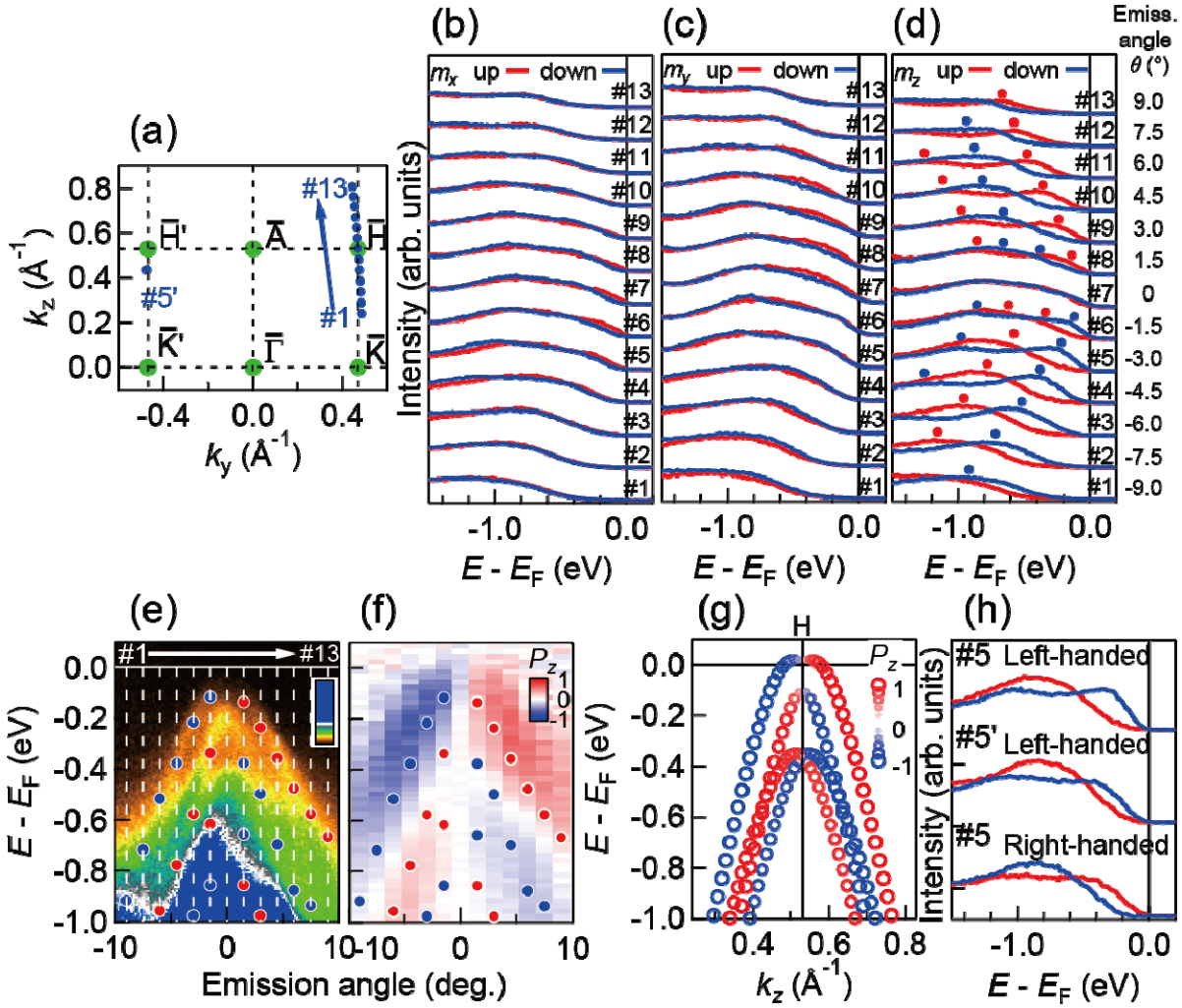

FIG. 3. (a) Two-dimensional Brillouin zone in Fig. 1(f) with the **k**-points (#1-#13, and #5' marked by blue circles) measured by SARPES. (b)-(d) Spin-resolved energy distribution curves (EDCs) for the spin magnetic moments along the *x, y,* and *z* axes defined in Fig. 1(a) (m_x, m_y and m_z), respectively, measured at $h\nu = 18$ eV for the left-handed crystal. Each EDC is labeled by #1-13 in (a). Hereafter, red (blue) color indicates the spin-up (down) component. The red and blue circles indicate the peak positions. (e) ARPES image recorded at $h\nu = 18$ eV. White lines represent the measurement cuts for the EDCs in (d). The markers indicate the peak positions plotted in (d). (f) SARPES image for the *z* component (P_z) of spin polarization for the left-handed crystal. The markers are the same as those in (e), indicating the peak positions plotted in (d). (g) Calculated spin polarizations along k_z (P_z). (h) Spin-resolved EDCs at #5 and #5' (around *H*- and *H*'-point, respectively) for the left-handed crystal, and at #5 (around *H*-point) for the right-handed crystal.

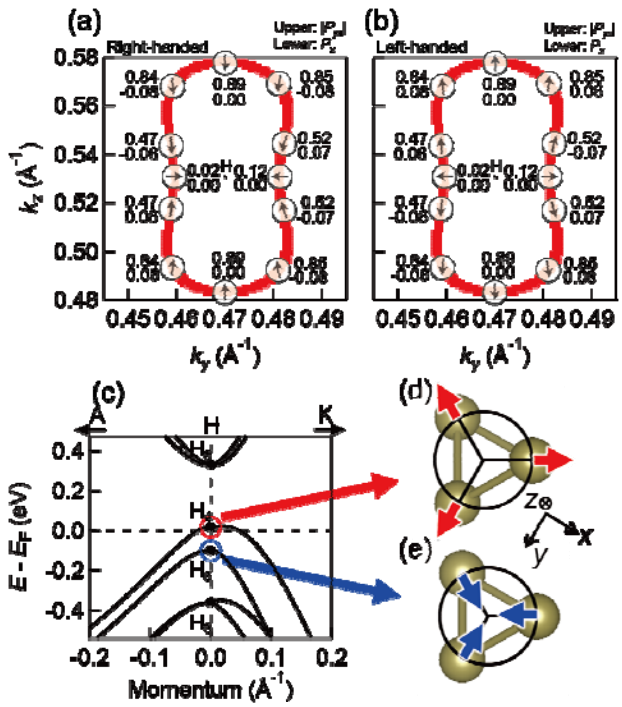

FIG. 4. (a), (b) Calculated Fermi surfaces along k_y-k_z formed 20 meV below VBM around the *H*-point for the right- and left-handed crystals, respectively. The arrows represent the directions of the in-plane polarization of the spin magnetic moment. The upper and lower numbers nearby the arrows indicate the absolute values of the in-plane and out-of-plane polarization ($|P_{yz}|$ and $P_{x,}$) of the spin magnetic moment, respectively. (c) The calculated band dispersions around the *H*-point. (d), (e) Top views of the spiral tellurium-chain. Red and blue arrows represent the symmetrically allowed spin polarizations just at the *H*-point for the eigenstates H_4 and H_5, respectively, mapped on the real space for the right-handed crystal. No net spin polarization is allowed at the *H*- and *H'*-points both in real- and **k**-space.